A Hybrid Transmitter-Based Efficiency Improvement Controller With Full-Bridge Dual Resonant Tank for Misalignment Condition

Ruikun Mai, *Member, IEEE*, Zhaotian Yan, *Student Member, IEEE*, Yang Chen, *Student Member, IEEE*, Shunpan Liu, and Zhengyou He, *Senior Member, IEEE*

***Abstract*—In general, misalignment in a wireless power transfer system is inevitable, which decreases the efficiency of the system. In this paper, a full-bridge dual resonant tank (FBDRT) topology is proposed to improve the system efficiency under the lateral-misalignment condition of a wireless power transfer system. The topology with two transmitters connected with two separate half bridges is employed to deliver power to the load. Operating principle, efficiency, current, power, and soft-switching region of the proposed method are analyzed in detail, and a comparison is drawn in with the traditional series–series topology. Theoretical analysis shows that the equivalent impedance of the transmitters can be adjusted, utilizing the phase-shift modulation. The proposed method holds a higher efficiency and a wider soft-switching region when the phase is selected reasonably. A 100 W prototype is built to validate the feasibility of the proposed topology. The efficiency of FBDRT is always higher than 88.3% with an improvement of 6.8%, compared with that of the traditional SS topology when the lateral misalignment increases from 0 to 200 mm (0%–50% of maximum coil size).**

***Index Terms*—Efficiency, full-bridge dual resonant tank, phase-shift modulation, soft-switching, wireless power transfer.**

I. Introduction

WIRELESS power transfer (WPT) based on magnetic coupling has been successfully employed in many applications, such as biomedical implants [1], underwater power supplies [2], mobile phones [3], electric vehicles [4]–[7], and even trains [8]. Among different performance parameters, efficiency has drawn the most attention from researchers [9], [10].

A WPT system, with a variable resistance of the load and a single transmitter (TX) and receiver (RX) will impact the efficiency of the system drastically. As a result, many researchers have focused on altering the equivalent load resistance to the optimal resistance in real time. For example, a dc–dc converter is used in the RX [11]–[13], and the equivalent load is changed to achieve a higher efficiency. However, such methods result in a complicated system. To avoid an additional dc–dc converter, the work [14] proposes a semi-bridge rectifier with which the maximum efficiency is achieved by pulse width modulation. Similarly, phase-shift modulation (PSM) of the rectifier is proposed in [15] to match the optimal load resistance. Nonetheless, the soft-switching characteristics of these systems are not studied in detail.

Multiple TXs can simultaneously operate for one RX, and the efficiency is increased in a specific space [16]–[19]. However, if the RX is close enough to a specific TX, the two-TX system might perform with a lower efficiency than the one-TX system [20]. Current in each TX can be adjusted to increase the system's efficiency [21], [22]. Current-controlled transmitting coils are proposed in [21], where a magnetic field is focused arbitrarily. Similarly, the current in TXs located at an arbitrary position can be adjusted by changing the amplitude ratio and phase difference of two TXs [22]. These results are summarized in [18], where the two-TX system was investigated under lateral-misalignment condition. The experiment shows that the coil current ratio should be equal to the coupling coefficient ratio to obtain the highest efficiency. However, these methods about multiple TXs systems not only complicate the system but also increase its cost.

A new dual-active-bridge, series resonant converter (DBSRC) with a dual tank is proposed in [23], and it beats the traditional DBSRC by optimizing the tap coefficient x of a tapped transformer. Such a structure can widen the zero voltage switching (ZVS) region and improve the efficiency through PSM, when the tap coefficient x changes. This paper implements this topology into a WPT system known as a full-bridge dual resonant tank (FBDRT), and its principle is transformed into the series-series (SS) topology with one TX under well-aligned condition. Even if the position of the RX changes, the proposed system presents a higher efficiency and a wider soft-switching region than the traditional SS topology.

This paper investigates the theoretical analysis of the optimal phase shift angle of a two-TX system, where the coupling between each TX and RX is different. The criterion for selecting a

Manuscript received December 20, 2018; revised March 22, 2019; accepted April 26, 2019. Date of publication May 9, 2019; date of current version October 18, 2019. This work was supported in part by the Fundamental Research Funds for the Central Universities under Grant 2682017QY01, in part by the National Key Research and Development Program of China under Grant 2017YFB1201002, in part by the National Natural Science Foundation of China under Grant 51677155, and in part by the National Science Fund for Distinguished Young Scholars under Grant 51525702. Recommended for publication by Associate Editor J. Acero. *(Corresponding author: Zhengyou He.)*

The authors are with the School of Electrical Engineering, Southwest Jiaotong University, Sichuan 611756, China (e-mail: mairk@swjtu.edu.cn; Zhaotian_Yan@163.com; yang.chen92@foxmail.com; liusp@my.swjtu.edu.cn; hezy@swjtu.edu.cn).

Color versions of one or more of the figures in this paper are available online at http://ieeexplore.ieee.org.

Digital Object Identifier 10.1109/TPEL.2019.2916231

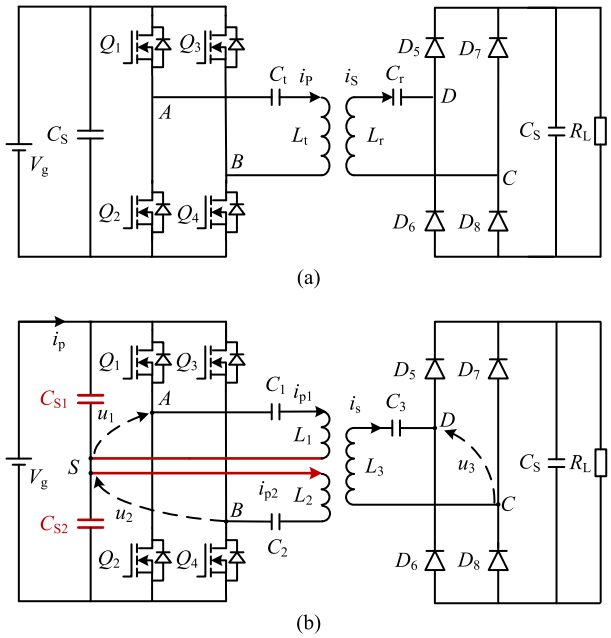

Fig. 1. (a) Traditional series-series topology. (b) The proposed FBDRT topology.

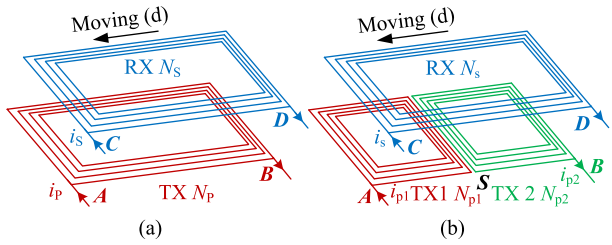

Fig. 2. (a) The structure of coupling model in the traditional SS topology. (b) The structure of the coupling model in the proposed FBDRT.

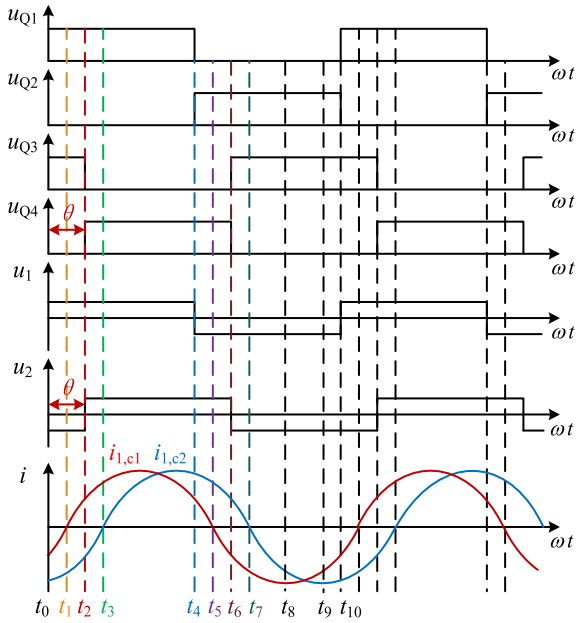

Fig. 3. Operating waveform of the proposed FBDRT.

phase shift angle at a certain position is studied to maximize efficiency. The topology and the principle of the proposed FBDRT are discussed in Section II. The system's modeling and its efficiency are derived and compared to the traditional SS topology in Section III. Section IV gives the current and power analysis of the proposed FBDRT. In Sections V and VI, soft-switching behavior and experimental results are given, respectively. The conclusion of the proposed work is drawn in Section VII.

II. Topology and Principle Analysis

Fig. 1(a) shows the traditional SS topology in a WPT system which is energized by MOSFETs Q_1–Q_4 and its antiparallel diodes in the TX. On the RX side, there are four diodes D_5–D_8, which can convert alternating current into direct current, while C_S is a capacitor stabilizing the input voltage. C_t (C_r) and L_t (L_r) are the compensation capacitor and self-inductance of the coil in TX and RX, respectively. The input voltage is V_g, whereas the load is R_L.

Fig. 1(b) represents the proposed FBDRT topology in a WPT, which has two symmetrical TXs with a single converter. The proposed approach requires splitting of the TX into two equal parts by connecting a wire in the middle of the TX. u_1 (u_2) is the voltage between points A and B. The variable i_{p1}, i_{p2}, and i_s are the currents in TX1, TX2, and RX, respectively. The positive direction of currents and voltages is provided in Fig. 1(b).

Fig. 2(a) demonstrates the structure of the traditional coupling model where the numbers of turns of the transmitting and receiving coils are N_P and N_S, respectively. Fig. 2(b) shows the coupling model of the FBDRT, where the transmitting coil L_t is divided into two coils, namely L_1 and L_2, and the turns of FBDRT are equal to that of the traditional SS topology, such as $N_{p1} = N_{p2} = N_P$ and $N_s = N_S$. The central tap of the transmitting coil and the midpoint (S) of the two slip capacitors are connected.

TX and RX are set to the same resonant frequency f. As shown in Fig. 3, u_{Q1}, u_{Q2}, u_{Q3}, and u_{Q4} are the driving signals in Q_1–Q_4. Two MOSFETs in one active bridge have a complemental signal, with 49.5% duty ratio (because of dead-band time). θ is the phase shift angle between two active bridges in TX. Therefore, there are ten states in one working period, which are analyzed as follows.

A. Interval 1: Before t_0

As shown in Fig. 4(a), only Q_3 is conducted at t_0 due to the dead-band time. Both the resonant currents, i_{p1} and i_{p2}, are negative. The current i_{p1} begins at point S and goes through C_1 and D_1. The resonant tank 1 regenerates energy to C_{S1}. The current i_{p2} starts from point S and goes through C_{S1}, Q_3, and C_2. Capacitor C_{S1} transfers energy to the resonant tank 2. During this period, both i_{p1} and i_{p2} will decrease in the negative direction.

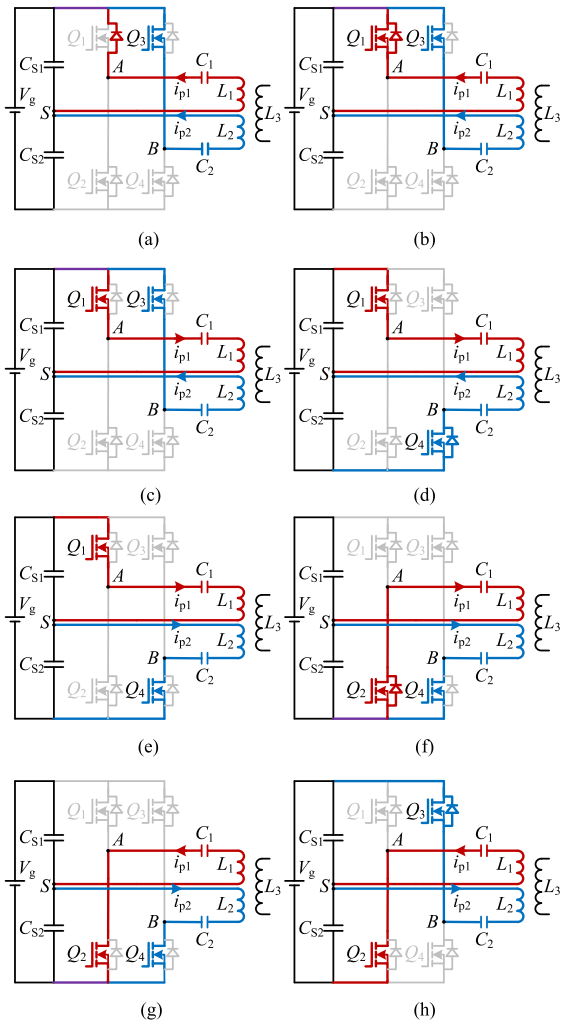

Fig. 4. Operating principle of the FBDRT in each interval: (a) Interval 1: before t_0. (b) Interval 2: t_0–t_1. (c) Interval 3: t_1–t_2. (d) Interval 4: t_2–t_3. (e) Interval 5: t_3–t_4. (f) Interval 6: t_4–t_5. (g) Interval 7: t_5–t_6. (h) Interval 8: t_6–t_7.

B. Interval 2: t_0–t_1

According to Fig. 4(b), the directions of the resonant currents (i_{p1} and i_{p2}) do not change. The current i_{p1} decreases to zero and Q_1 is switched ON with ZVS. Resonant tank 1 feeds energy to C_{S1}, and in turn, C_{S1} delivers energy to tank 2. i_{p1} and i_{p2} will continue to decrease in the negative direction.

C. Interval 3: t_1–t_2

As shown in Fig. 4(c), Q_1 and Q_3 are conducting during t_1–t_2. The resonant current i_{p1} is positive, while i_{p2} is negative. The current i_{p1} begins at point S and goes through C_{S1}, Q_1, and C_1. Capacitor C_{S1} transfers energy to resonant tanks 1 and 2. i_{p1} increases in a positive direction while i_{p2} continues to decreases in a negative direction.

D. Interval 4: t_2–t_3

During period t_2 to t_3 as shown in Fig. 4(d), the directions of the resonant currents i_{p1} and i_{p2} do not change, an di_{p1} is positive while i_{p2} is negative. Q_4 is switched ON with ZVS at t_2 and the current i_{p2} decreases to zero at t_3. C_{S1} transfers energy to resonant tank 1 while resonant tank 2 regenerates energy to C_{S2}. i_{p1} increases in a positive direction while i_{p2} decreases in a negative direction.

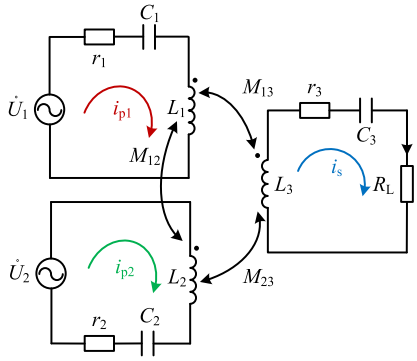

Fig. 5. The equivalent circuit of the FBDRT in WPT.

E. Interval 5: t_3–t_4

As shown in Fig. 4(e), the direction of resonant current i_{p1} does not change, whereas i_{p2} becomes positive. The current i_2 begins at point S and goes through C_2 and Q_4. The capacitors C_{S1} and C_{S2} transfer energy to resonant tanks 1 and 2.

F. Interval 5: t_4–t_5

In this interval, both the resonant currents do not change directions, and Q_2 is switched ON with ZVS at t_4. The current i_{p1} begins from point S and goes through the capacitor C_{S2}, D_2, and C_1. Resonant tank 1 regenerates energy to capacitor C_{S2}, and in turn, C_{S2} delivers energy to resonant tank 2. As a result, i_{p1} will decrease while i_{p2} will increase.

G. Interval 6: t_5–t_6

In this interval, resonant current i_{p1} changes the direction. The current i_{p2} begins from point S and goes through C_1, Q_2, and C_{S2}. Meanwhile, capacitor C_{S1} delivers energy to resonant tanks 1 and 2.

H. Interval 6: t_6–t_7

Fig. 4(h) shows the condition from t_6 to t_7. The direction of resonant currents i_{p1} and i_{p2} does not change, and Q_3 is switched ON with ZVS at t_6. Capacitor C_{S2} transfers energy to resonant tank 1, and resonant tank 2 regenerates energy to the capacitor C_{S1}.

Similarly, t_7–t_{10} can be analyzed in the same manner as t_0–t_6. FBDRT can realize the ZVS condition in TX (Q_1–Q_4) if the voltages u_1 and u_2 are ahead of the currents, i_{p1} and i_{p2}.

III. Modeling and Efficiency Analysis

A. Modeling of the FBDRT

The FBDRT's equivalent circuit is shown in Fig. 5 to analyze its characteristics. r_1, r_2, and r_3 are the parasitic resistances of TX1, TX2, and RX, respectively. M_{ij} is the mutual inductance

between L_i and L_j ($i, j \in [1, 3]$ and $i \neq j$). For simplification purposes, the parasitic resistances of the capacitors and skin effect of the Litz wire are ignored.

The TX can be seemed as being driven by two AC voltage sources $\dot{U}_1$ and $\dot{U}_2$, which have the same amplitude but different phase shift angles (θ). The following equation shows the relationship between $\dot{U}_1$, $\dot{U}_2$, and V_g:

$$\begin{cases} \dot{U}_1 = \frac{2V_g}{\pi}\angle 0 = U\angle 0 \\ \dot{U}_2 = \frac{2V_g}{\pi}\angle\theta = U\angle\theta. \end{cases} \tag{1}$$

The voltages $\dot{U}_1$, $\dot{U}_2$ and the currents $\dot{I}_{p1}$, $\dot{I}_{p2}$, and $\dot{I}_s$ are assumed to be sinusoidal. According to Kirchhoff's Voltage Law, the matrix equation can be obtained as follows:

$$\begin{bmatrix} Z_1 & j\omega M_{12} & -j\omega M_{13} \\ j\omega M_{12} & Z_2 & -j\omega M_{23} \\ -j\omega M_{13} & -j\omega M_{23} & Z_3 \end{bmatrix} \cdot \begin{bmatrix} \dot{I}_{p1} \\ \dot{I}_{p2} \\ \dot{I}_s \end{bmatrix} = \begin{bmatrix} \dot{U}_1 \\ \dot{U}_2 \\ 0 \end{bmatrix}. \tag{2}$$

ω is the angular frequency of the system, and the system's frequency is set at $f = 85$ kHz. Z_1, Z_2, and Z_3 are the impedances of each resonant tank while TXs have the same structure as in Fig. 2. The parameters are given in (3).

$$\begin{cases} Z_1 = Z_2 = r + \omega L + \frac{1}{j\omega C} \\ Z_3 = r_3 + R_L + \omega L_3 + \frac{1}{j\omega C_3}. \end{cases} \tag{3}$$

The relationship between inductors and capacitors of resonant tanks are described by

$$\omega L_i + \frac{1}{j\omega C_i} = 0, i = 1, 2, 3. \tag{4}$$

The currents in TXs and RX can be solved according to (2), as follows:

$$\begin{cases} \dot{I}_{p1} = \frac{U}{\varepsilon} \cdot [(c + dj)\sin(\theta) + (d - cj)\cos(\theta) + (\alpha + \beta j)] \\ \dot{I}_{p2} = \frac{U}{\varepsilon} \cdot [(e + fj)\sin(\theta) + (f - ej)\cos(\theta) + (d - cj)] \\ \dot{I}_s = \frac{U}{\varepsilon} \cdot [(a + bj)\sin(\theta) + (b - aj)\cos(\theta) + (g + hj)] \end{cases} \tag{5}$$

where the symbols are given in the Appendix.

B. System Efficiency Analysis

The power equations of the FBDTR can be written as (6), in which P_{in1} and P_{in2} (P_{out}) are the power delivered (received) by TX1 and TX2 (RX), respectively.

$$\begin{cases} P_{\text{in1}} = \frac{1}{2} \cdot \text{Re}(\dot{U}_1 \cdot \dot{I}_{p1}^*) = \frac{U^2}{2\varepsilon}[c\sin(\theta) + d\cos(\theta) + \alpha] \\ P_{\text{in2}} = \frac{1}{2}\text{Re}(\dot{U}_2 \cdot \dot{I}_{p2}^*) = \frac{U^2}{2\varepsilon}[d\cos(\theta) - c\sin(\theta) + f] \\ P_{\text{out}} = \frac{1}{2}\dot{I}_s \cdot \dot{I}_s^* \cdot R_L = \frac{U^2}{2\varepsilon}[A\sin(\theta) + B\cos(\theta) + C] \end{cases} \tag{6}$$

where

$$\begin{cases} A = 2rR_L\omega^3 M_{12}({M_{13}}^2 - {M_{23}}^2) \\ B = 2R_L\omega^2 M_{13}M_{23}(r^2 + \omega^2 {M_{12}}^2) \\ C = R_L\omega^2({M_{13}}^2 + {M_{23}}^2)(r^2 + \omega^2 {M_{12}}^2). \end{cases}$$

TABLE I
PARAMETERS OF FBDRT FOR SIMULATION

Description	Parameter
Input voltage (V_g) /V	60
Resonant frequency(f_s) /Hz	85000
Loss resistance 1&2(r) /Ω	0.4
Loss resistance 3(r_3) /Ω	0.6
Load (R_L) /Ω	40

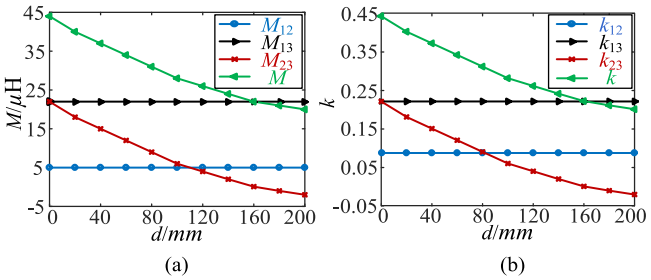

Fig. 6. (a) The mutual inductance of the FBDRT (M_{12}, M_{13}, and M_{23}) and the traditional SS topology (M). (b) The coupling coefficient of the FBDRT (k_{12}, k_{13}, and k_{23}) and the traditional SS topology (k).

The input power can be written as $P_{\text{in}} = P_{\text{in1}} + P_{\text{in2}}$. Therefore, the system efficiency (η) can be obtained as

$$\eta = \frac{P_{\text{out}}}{P_{\text{in}}} = \frac{A\sin(\theta) + B\cos(\theta) + C}{2d\cos(\theta) + \alpha + f}. \tag{7}$$

According to (7), η has no relationship to the input voltage V_g while it is a function against the mutual inductances M_{12}, M_{13}, M_{23}, and θ. There exists a maximum value of η at a certain misalignment while θ is varying from 0 to 2π. Equation (8) takes the derivative of η (θ).

$$\frac{\mathrm{d}\eta}{\mathrm{d}\theta} = \frac{A(f + \alpha)\cos(\theta) + (2dC - B\alpha - Bf)\sin(\theta) + 2dA}{[2d\cos(\theta) + \alpha + f]^2}. \tag{8}$$

Equation (8) equals to zero so that η obtains a maximum value ($\eta_{\max}$) on condition that $\theta = \theta_{\max}$. $\theta_{\max}$ is a function of mutual inductance and misalignment distance (d), as shown in (9).

$$\theta_{\max} = f(M_{12}, M_{13}, M_{23}) = g(d). \tag{9}$$

To analyze the characteristics of the system, the parameters of components are depicted in Table I.

As the RX moves horizontally, the mutual inductances of the FBDRT and the traditional SS topology will change, which can be obtained by ANSYS MAXWELL. Results show that the variation of M_{13} and M_{12} are very small compared to that of M_{23} so that M_{13} and M_{12} can be viewed as constants to simplify the operation. M can be regarded as the sum of M_{13} and M_{23}. Fig. 6 shows the variations of the mutual inductance and the coupling coefficient, when the RX moves horizontally towards TX1, $k_{ij} = M_{ij}/\sqrt{L_i L_j}$ ($i, j = 1, 2, 3$).

System's efficiency versus angle θ with different d is shown in Fig. 7. FBDRT can maintain maximum efficiency with different misalignment distances by using the optimized θ. At a certain misalignment, the efficiency of the system is related to θ and load R_L. Fig. 8 shows the efficiency variation when the misalignment

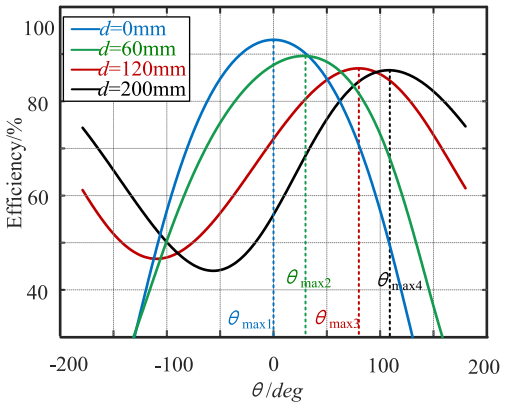

Fig. 7. Efficiency varying with θ at the different level position ($R_L = 40$).

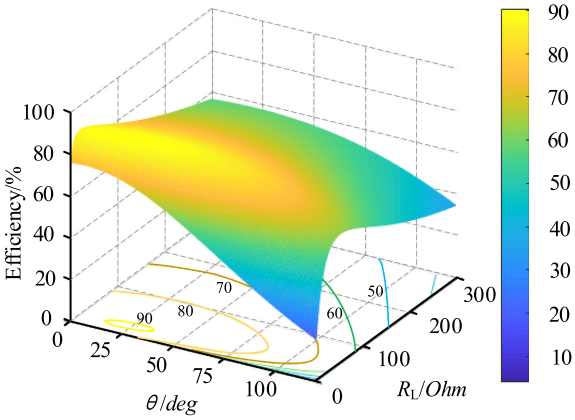

Fig. 8. Efficiency varying with θ and the load R_L when $d = 60$ mm ($k_{13}/k_{23} = 1.8$).

distance is 60 mm ($k_{13}/k_{23} = 1.8$), and there exist an optimal load R_L and angle θ.

M_{13} will be equal to M_{23}, on condition that $d = 0$, so that the current in TXs will be same. Therefore, the middle wire that connects point S with the transmitting coil can be taken away to make it like a traditional SS topology. The parameters of the main components are shown in (10).

$$\begin{cases} M = M_{13} + M_{23} \\ M_{12} = 0 \\ \varphi_{AB} = 0. \end{cases} \tag{10}$$

Taking these parameters into (7), the paper gives the efficiency of the traditional SS topology

$$\eta_t = \frac{P_{\text{out}}}{P_{\text{in}}} = \frac{\omega^2 M^2 R_L}{(r_3 + R_L)[2(r_3 + R_L)r + \omega^2 M^2]}. \tag{11}$$

Fig. 9 shows the maximum efficiency curve of FBDRT and traditional SS topology with different misalignment conditions, where the loads are 40, 80, and 120 Ω, respectively. FBDRT can maintain a higher efficiency utilizing PSM, while the efficiency of traditional SS topology decreases rapidly.

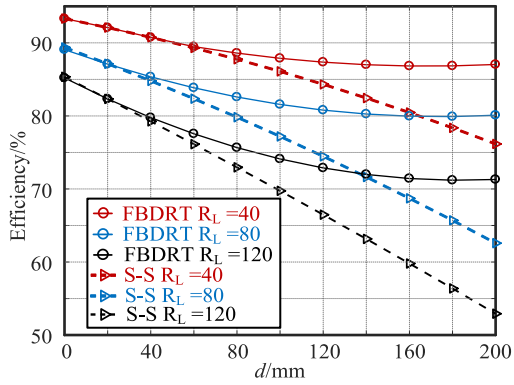

Fig. 9. Efficiencies of FBDRT compared with traditional SS topology.

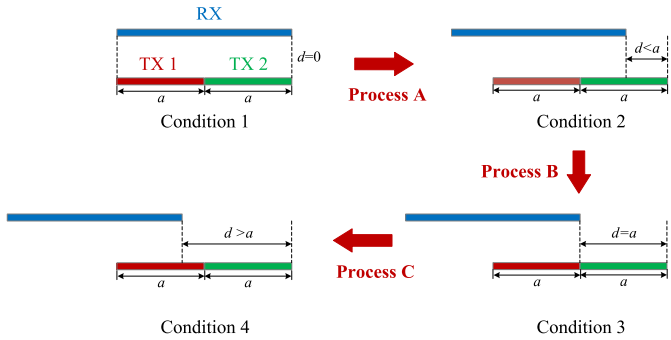

Fig. 10. The condition and the progress of moving the RX to TX1.

TABLE II
TOLERANCE LIMITATION OF FBDRT

Process	Mutual inductance			State
	M_{12}	M_{13}	M_{23}	
A	Constant	Constant	Decrease	Valid
B	Constant	Constant	Decrease	Valid
C	Constant	Decrease	Decrease	Invalid

C. The Range of Misalignment

It is necessary to illustrate the range of misalignment tolerance, and the event can be analyzed as three processes, as shown in Fig. 10. The mutual inductance will fluctuate in the process of moving so that the PSM should be adopted to distribute the energy transferred by two TXs which undertake the same energy transmission in condition 1. TX1 will work as the main energy transmission channel with RX close to TX1 and vice versa. However, such method has a tolerance limitation, as shown in Table II.

In order to verify the range of misalignment, the mutual inductance at a different position is taken into (7), and the efficiency curves can be drawn as Fig. 11, where the loads are 40, 80, and 120 Ω, respectively.

According to Fig. 11, the range of misalignment can be summarized as $-a \le d \le a$, where a is the size of the transmitting coil ($a = 200$ mm).

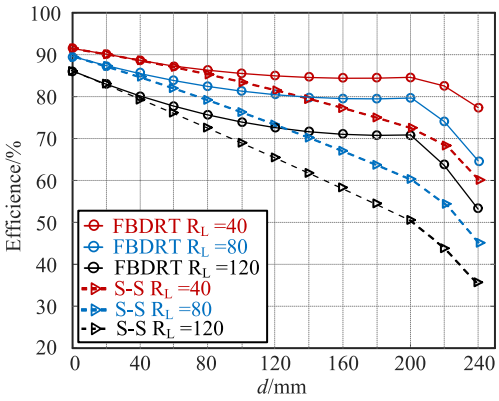

Fig. 11. Efficiencies of FBDRT under misalignment condition ($a = 200$ mm).

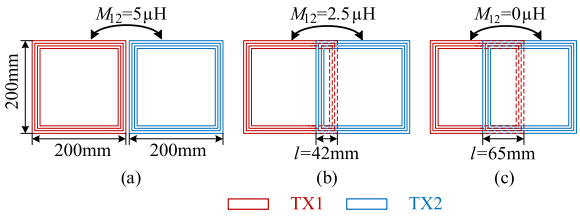

Fig. 12. The value of M_{12} when two transmitting coils are placed in different positions.

D. The Effect of M_{12} on Efficiency

The mutual inductance between TXs (M_{12}) will influence the efficiency. In order to illustrate the relationship between the system's efficiency and M_{12}, the paper introduces the BPP structure which consists of two identical, partially overlapped and mutually decoupled coils [24]. The mutual decoupling of the coils constituting the BPP is achieved by adjusting the overlap of the two coils, and the mutual inductance between the two coils depends on the extent of overlap, as shown in Fig. 12.

l is the length of the overlap of the two coils. There is no change in coil size so that the fluctuation of M_{13} and M_{23} is very small when the transmitting coils are placed in Fig. 12.

The previous theoretical derivation was based on no overlapping between the transmitting coils, as shown in Fig. 12(a). Take the value of M_{12} into (7), and the efficiency versus phase shift angle θ at different misalignment conditions can be shown as follows.

According to Fig. 13(a), the maximum efficiency is the same under well-aligned condition ($d = 0$ mm) while it will drop down with M_{12} decrease when the lateral misalignment occurs, as shown in Fig. 12(b). Namely, the system will get a better condition if M_{12} is greater.

Furthermore, the extreme value of efficiency is unrelated to the phase shift angle θ, when two transmitting coils are decoupled ($M_{12} = 0$). Therefore, the efficiency will get its maximum value when $\theta = 0$, as shown in Fig. 14.

Fig. 15(a) shows the maximum efficiency curves of FBDRT with different misalignment conditions where M_{12} is 0, 2.5, and 5 μH, respectively. Fig. 15(b) shows the efficiencies of FBDRT varying with M_{12} at three positions, and efficiency is improved significantly when M_{12} increases.

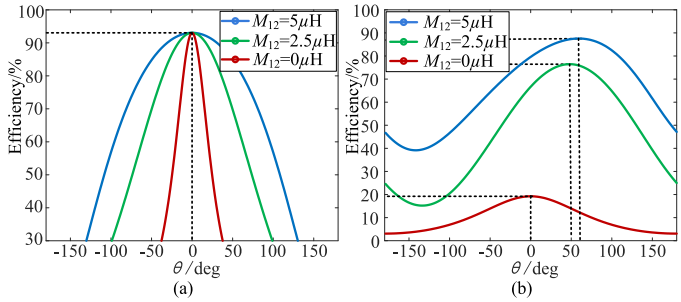

Fig. 13. (a) Efficiency varying with θ and M_{12} ($d = 0$ mm). (b) Efficiency varying with θ and M_{12} ($d = 100$ mm).

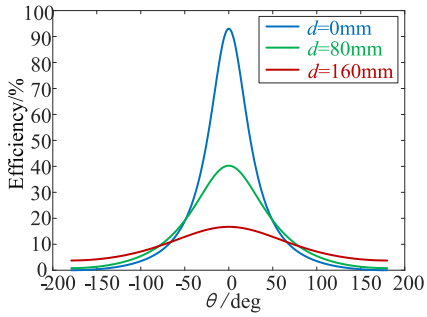

Fig. 14. Efficiency varying with θ when transmitting coils are decoupled ($M_{12} = 0$) when the lateral misalignment occurs.

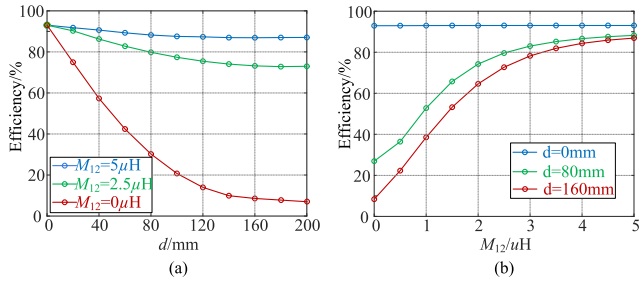

Fig. 15. (a) Efficiencies of FBDRT under the different value of M_{12} ($R_L = 40\,\Omega$). (b) Efficiencies of FBDRT varying with M_{12} at three positions ($R_L = 40\,\Omega$).

IV. Current and Power

A. Current in FBDRT and Traditional SS Topology

According to (5), the rms value of currents in FBDRT can be derived as follows:

$$\begin{cases} I_{p1} = \dfrac{|\dot{I}_{p1}|}{\sqrt{2}} \\ I_{p2} = \dfrac{|\dot{I}_{p2}|}{\sqrt{2}} \\ I_s = \dfrac{|\dot{I}_s|}{\sqrt{2}}. \end{cases} \tag{12}$$

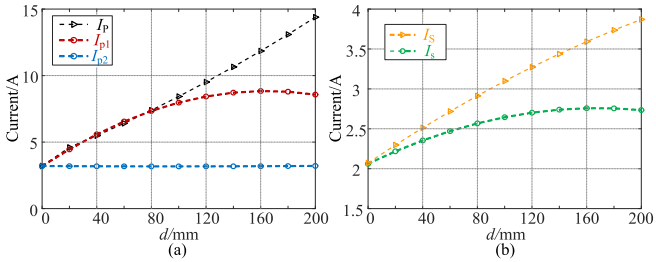

Fig. 16. (a) The current variation of transmitters in the proposed FBDRT and the traditional SS topology. (b) The current variation of receivers in the proposed FBDRT and the traditional SS topology.

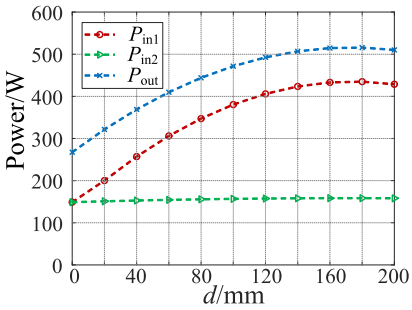

Fig. 17. The variation of the power in FBDRT.

Similarly, according to (10) and Kirchhoff's Voltage Law, the rms currents in traditional SS topology can be described as

$$\begin{cases} I_P = \frac{\sqrt{2}U(r_3+R_L)}{2(r_3+R_L)r+\omega^2M^2} \\ I_S = \frac{\sqrt{2}\omega MU}{2(r_3+R_L)r+\omega^2M^2}. \end{cases} \tag{13}$$

I_P and I_S are the rms current of the transmitting coil and the receiving coil in the traditional SS topology. In both traditional SS topology and proposed FBDRT topology, the currents in transmitters and receiver will increase under the misalignment condition because of the fluctuation of mutual inductance, as shown in Fig. 16.

Fig. 16(a) shows the currents variation of transmitters in FBDRT and traditional SS topology, respectively, while Fig. 16(b) shows that of receivers. When the RX is close to TX1, TX1 will serve as the main energy transmission channel so that the current in TX1 will increase through the proposed PSM. However, the currents in the traditional SS topology are uncontrollable, and the variation in currents of the traditional SS topology is bigger than that of the proposed FBDRT topology apparently. Namely, the proposed FBDRT has better constant current characteristics, and the current stress can be lightened.

B. Power in FBDRT

According to (6), P_{in1}, P_{in2}, and P_{out} of FBDRT are shown in Fig. 17. It is clear that the variation trend of power is the same as that of currents.

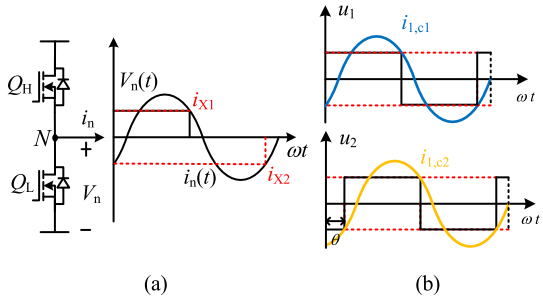

Fig. 18. (a) Voltage and current waveform of one leg. (b) Voltage and current waveform of TX1 and TX2.

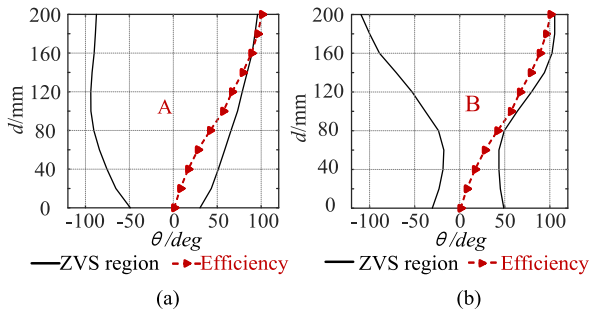

Fig. 19. ZVS condition of the proposed FBDRT: (a) ZVS for leg A when level position varies from 0 to 200 mm (region A is the ZVS region for leg A), (b) ZVS for leg B (region B is the ZVS region for leg B).

V. Analysis of Soft-Switching

Both the proposed FBDRT topology and the traditional SS topology have two bridge legs in the inverter. Each bridge leg in TX has an equivalent circuit. Fig. 18(a) gives the ZVS condition for one leg, whereas $V_n(t)$ is the voltage of the point N. In [23], the ZVS condition for one leg is given as $i_{X1} > 0$, $i_{X2} < 0$.

The proposed FBDRT has two TXs. The relationship between the voltage and current in two TXs is shown in Fig. 18(b). It can be found that if u_i is ahead of i_{pi} $(i = 1, 2)$, legs A and B can work in a ZVS condition.

$$\begin{cases} \varphi_1 = \arg(\frac{\dot{U}_1}{\dot{I}_{p1}}) > 0 \\ \varphi_2 = \arg(\frac{\dot{U}_2}{\dot{I}_{p2}}) > 0. \end{cases} \tag{14}$$

The phase angles φ_1 and φ_2 between the voltage and the current in two TXs can be expressed as (12), which gives the ZVS condition of legs A and B.

With the increase of d, ZVS condition changes due to the variation of the mutual inductance and θ. The mutual inductance (Fig. 6) can be substituted into (12), and the ZVS condition is recalculated. Fig. 19(a) shows the relationship between the ZVS region of leg A and the maximum efficiency curve at different positions. Black lines are the boundaries of ZVS region, while the red line is the maximum efficiency curve at a different position.

Similarly, region B is also a ZVS region and black lines are the boundaries in Fig. 19(b). It can be found that both legs A

TABLE III
ZVS CONDITION OF FBDRT IN DIFFERENT POSITIONS

d/mm	0-160 (0-40%)	160-200 (40%-50%)
ZVS condition	Leg A &Leg B	Leg B

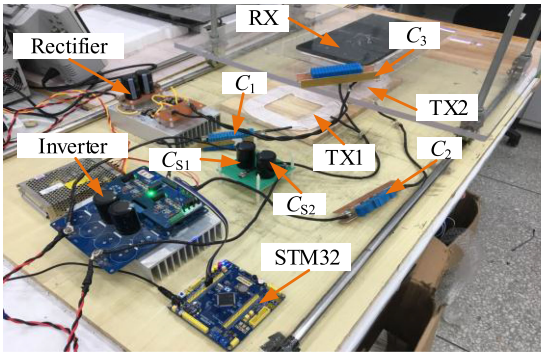

Fig. 20. The experimental setup.

TABLE IV
PARAMETERS OF FBDRT FOR EXPERIMENT

Description	Parameter
Input voltage (V_g) / V	60
Resonant frequency (f_s) / Hz	85000
Capacitor 1 (C_1) / nF	60.8
Capacitor 2 (C_2) / nF	63.3
Capacitor 3 (C_3) / nF	20.2
Capacitor S1 (C_{S1}) / μF	470
Capacitor S2 (C_{S2}) / μF	470
Load (R_L) / Ω	40
Inductance 1 (L_1) / μH	57.7
Inductance 2 (L_2) / μH	55.4
Inductance 3 (L_3) / μH	173.5

and B have different ZVS regions. The conclusion of the ZVS of FBDRT is drawn in Table III.

VI. EXPERIMENT RESULTS

As shown in Fig. 20, a prototype WPT system is set up to verify the proposed topology according to the parameters in Table IV. SiC MOSFETs (C2M0160120D) are chosen as the switches in the inverter. There is only one inverter with a single dc input source (IT6526D) in TX. The gate drives the signal, and the PSM is generated by the STM32F103. The RX coil is connected to the rectifier and an electronic load (IT8818BS) serves as a load resistor. The air gap between the TX and RX is 6.0 cm, while RX is covered with ferrite cores.

The appearance of TX and RX is shown in Fig. 21(a). The dimensions of TXs and RX are 20 cm × 20 cm and 20 cm × 40 cm, respectively. The turns of TX and RX coils are equal, i.e., $N_{p1} = N_{p2} = N_s = 17$. The measured parasitic resistance is 0.4 Ω of one transmitting coil and 0.6 Ω of the receiving coil. The coil is wounded by Litz wire of 3 mm × 600 strands. The mutual inductance with misalignment of FBDRT is shown in Fig. 21(b).

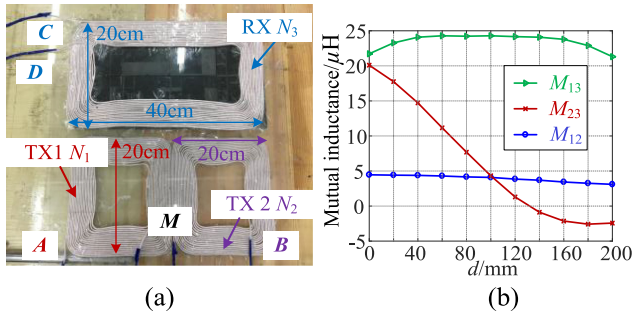

Fig. 21. (a) Coils in the TXs and the RX of FBDRT. (b) The FBDRT's mutual inductance with misalignment.

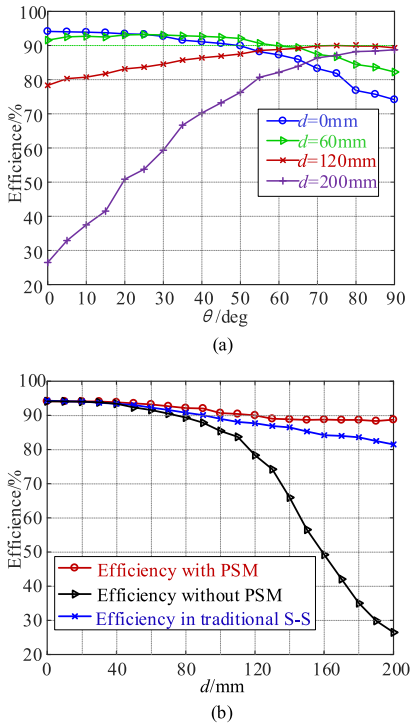

Fig. 22. (a) The efficiency curves of FBDRT with $R_L = 40\,\Omega$. (b) The efficiency variation about FBDRT with PSM, FBDRT without PSM, and traditional SS topology at different positions.

Fig. 22(a) gives the efficiency curves of FBDRT with $R_L = 40\,\Omega$. The RX is placed at 0, 60, 120, and 200 mm from TXs, while θ changes from 0 to $\pi/2$. The maximum efficiency is different in every curve. Fig. 22(b) gives the maximum efficiency curve of FBDRT with PSM, without PSM in FBDRT, and with traditional SS topology. The performance of FBDRT with PSM is better than that of the traditional SS topology. For the FBDRT, the maximum efficiency is 94.13% when $d = 0$ and is higher than 88.3%, provided the RX moves from 0 to 200 mm.

The BPP structure is introduced in this experiment, and the mutual inductance between the two coils (M_{12}) depends on the extent of overlap, as shown in Fig. 12. However, it is impossible to decouple the two coils completely in the experiment. The efficiency versus phase shift angle θ is measured where M_{12} is 0.22, 2.45, and 4.82 μH, respectively, as shown in Fig. 23.

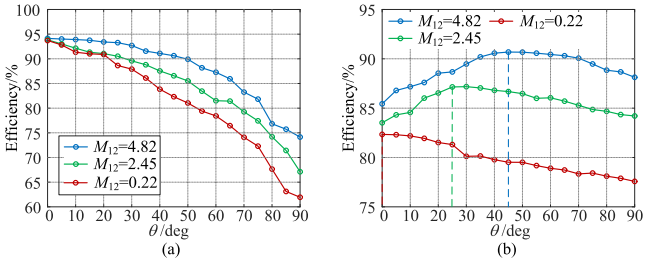

Fig. 23. (a) Efficiency varying with θ and M_{12} ($d = 0$ mm). (b) Efficiency varying with θ and M_{12} ($d = 100$ mm).

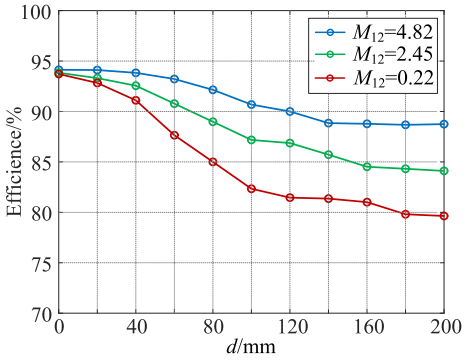

Fig. 24. Efficiencies of FBDRT under the different value of M12 ($R_L = 40\,\Omega$).

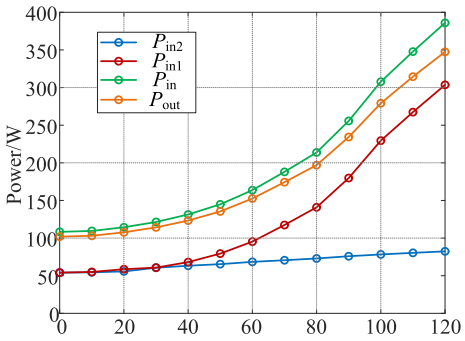

Fig. 25. The variation of the power in FBDRT.

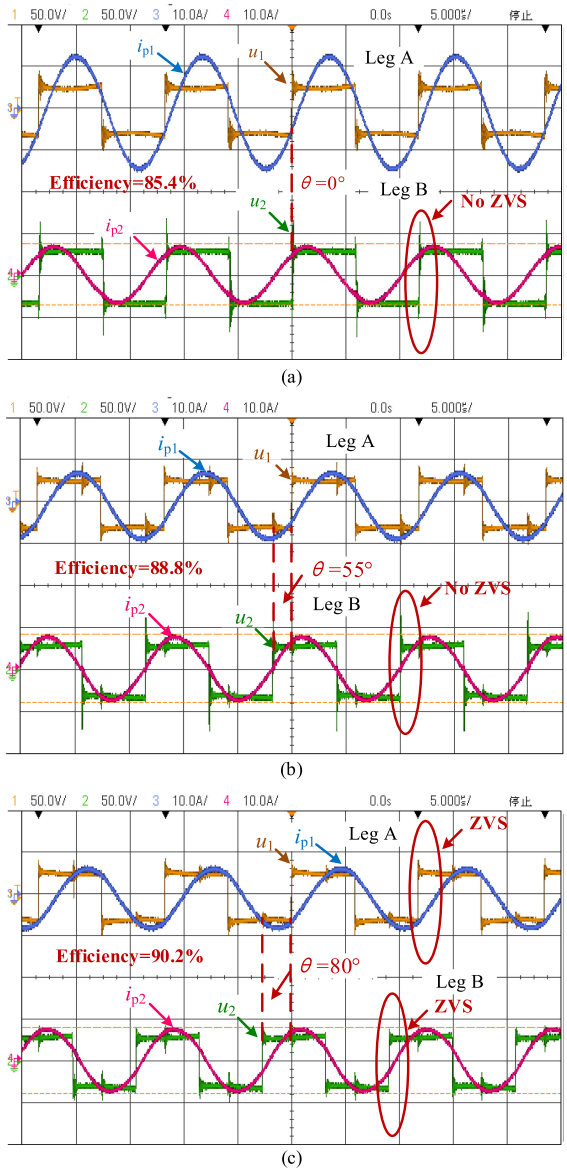

Fig. 26. (a) The experimental waveforms of voltages u_1, u_2, and currents i_{p1}, i_{p2} when $d = 120$ mm and $\theta = 0°$. (b) The experimental waveforms of voltages u_1, u_2, and currents i_{p1}, i_{p2} when $d = 120$ mm and $\theta = 55°$. (c) The experimental waveforms of voltages u_1, u_2, and currents i_{p1}, i_{p2} when $d = 120$ mm and $\theta = 80°$.

Fig. 24 shows the maximum efficiency curves of FBDRT with different misalignment conditions where M_{12} is 0.22, 2.45, and 4.82 μH, respectively. The efficiency will drop sharply if M_{12} decreases.

Fig. 25 shows the power variation of TX1, TX2, input, and output in FBDRT. When the RX is close to TX1, TX1 will serve as the main energy transmission channel so that the current in TX1 will increase through the proposed PSM.

The experimental waveforms of voltages u_1, u_2, and currents i_{p1}, i_{p2} can be seen in Fig. 26, with the operating conditions of $V_g = 80$ V, $R_L = 40\,\Omega$, and $d = 120$ mm. Currents in TX1 and TX2 are unbalanced when $\theta = 0°$ and the switching loss is high. Leg A will realize ZVS condition and the switching loss of leg B will be smaller when $\theta = 55°$. The efficiency can reach its maximum value of 90.2% at $\theta = 80°$. Legs A and B can both realize ZVS at maximum efficiency.

The system is inevitably disturbed in practical applications, which causes the voltage fluctuation at point S, and the rms values of U_1 and U_2 are not the same. Therefore, it is necessary to analyze the voltage fluctuation at point S.

The initial voltages of the C_{S1} and C_{S2} are set to the different values, and the voltage of C_{S2} is equal to that of point S. Fig. 27 shows the voltages fluctuation of U_{CS1}, U_{CS2}, and U_S. The initial voltages of C_{S1} (C_{S2}) are set to 30 V (30 V) and 20 V (40 V), respectively (between point O and point A). The system starts running at point A, and the voltage at point S (U_S) does not change within the time of observation (128 and 132 s).

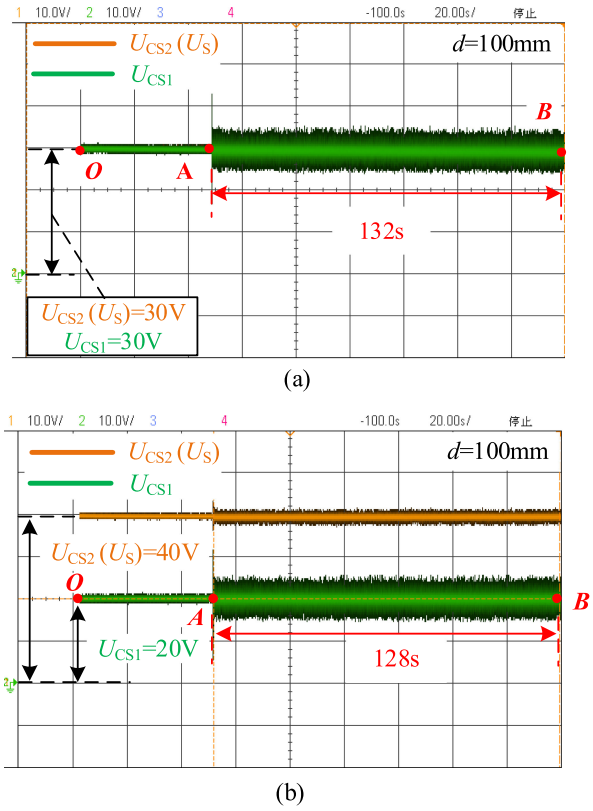

Fig. 27. (a) The voltages fluctuation value of U_{CS1}, U_{CS2}, and U_S ($U_{CS1} = U_{CS2} = 30$ V). (b) The fluctuation value of the U_{CS1}, U_{CS2}, and U_S ($U_{CS1} = 20$ V, $U_{CS2} = 40$ V).

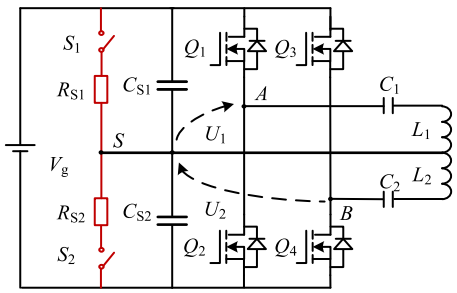

Fig. 28. The improved topology to balance the voltage of C_{S1} and C_{S2}.

Though the rms values of U_1 and U_2 are not always the same, the system will not crash if the *S*-point voltage fluctuates. It is necessary to balance the voltage on the two capacitors (C_{S1} and C_{S2}) so that the proposed theoretical derivation can work.

The method which can balance the voltages at point *S* can be shown as Fig. 28. The two resistors are paralleled at C_{S1} and C_{S2}, and the resistance of R_{S1} and R_{S2} is equal. The paralleling resistors provide an energy path when the voltage fluctuates between the two capacitors (C_{S1} and C_{S2}).

The waveform is shown in Fig. 29. During point *O* and point *A*, the initial voltage of C_{S1} and C_{S2} is 40 and 20 V, respectively. At point *A*, the system begins to operate, and the voltage of the two capacitors is unequal. At point *B*, the switches S_1 and S_2

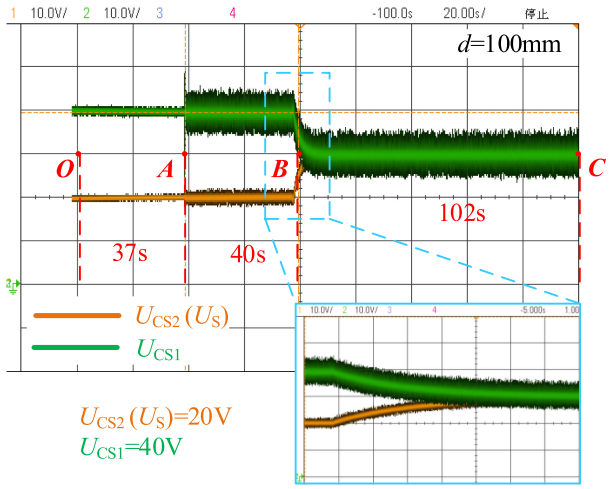

Fig. 29. The voltage fluctuation of C_{S1} and C_{S2} when $d = 100$ mm.

turn on so that the voltage at point *S* can be balanced. In the experiment, R_{S1} and R_{S2} are all 5.1 kΩ, and C_{S1} and C_{S2} are 470 μF. The power loss of the resistance is about 0.35 W in the experiment, which shows the little effect on the system's efficiency (the output power of the system is above 100 W).

The voltage balance time is related to the value of C_{S1}, (C_{S2}), and R_{S1}, (R_{S2}), and the time constant τ can be defined as follows:

$$\tau = R_{S1} \cdot C_{S1} = R_{S2} \cdot C_{S2}. \tag{15}$$

The voltage balance time will be longer if τ gets a large value. In this experiment, the voltage balance time is about 5 s.

VII. Conclusion

In this paper, FBDRT topology is proposed to improve efficiency when lateral misalignment occurs in a WPT system. According to the theoretical analysis, PSM is applied to TXs, and ZVS condition can be achieved. The equivalent impedance of two TXs is adjusted at different positions, and there is an obvious improvement in efficiency compared to the traditional SS topology. The proposed method is validated by a 100 W experimental prototype. The experimental results show that the efficiency in comparison to the traditional SS topology is always higher than 88.3% with an improvement of 6.8% when the RX moves from 0 to 200 mm (0%–50% of maximum coil size).

Appendix

Symbols in Section III can be written as follows:

$$\begin{cases} \varepsilon = [(r_3 + R_L)(\omega^2 {M_{12}}^2 + r^2) + r\omega^2({M_{13}}^2 + {M_{23}}^2)]^2 \\ \quad + 4\omega^6 {M_{12}}^2 {M_{13}}^2 {M_{23}}^2 \\ \alpha = [\omega^2 {M_{23}}^2 + r(r_3 + R_L)][r\omega^2({M_{13}}^2 + {M_{23}}^2) \\ \quad + (r^2 + \omega^2 {M_{12}}^2)(r_3 + R_L)] \\ \beta = 2\omega^3 M_{12} M_{13} M_{23}[\omega^2 {M_{23}}^2 + r(r_3 + R_L)] \end{cases} \tag{A.1}$$

$$\begin{cases} a = -r\omega M_{23}[r\omega^2({M_{13}}^2 + {M_{23}}^2) + (r^2 + \omega^2{M_{12}}^2)(r_3 + R_L)] - 2\omega^5{M_{12}}^2{M_{13}}^2M_{23} \\ b = \omega^2M_{12}M_{13}[r\omega^2({M_{13}}^2 - {M_{23}}^2) + (r^2 + \omega^2{M_{12}}^2)(r_3 + R_L)] \\ c = \omega M_{12}(r_3 + R_L)[r\omega^2({M_{13}}^2 + {M_{23}}^2) + (r^2 + \omega^2{M_{12}}^2)(r_3 + R_L)] + 2\omega^5M_{12}{M_{13}}^2{M_{23}}^2 \\ d = -\omega^2M_{13}M_{23}[r\omega^2({M_{13}}^2 + {M_{23}}^2) + (r^2 - \omega^2{M_{12}}^2)(r_3 + R_L)] \end{cases} \tag{A.2}$$

$$\begin{cases} e = -2\omega^3M_{12}M_{13}M_{23}[\omega^2{M_{13}}^2 + r(r_3 + R_L)] \\ f = [\omega^2{M_{13}}^2 + r(r_3 + R_L)][r\omega^2({M_{13}}^2 + {M_{23}}^2) + (r^2 + \omega^2{M_{12}}^2)(r_3 + R_L)] \\ g = \omega^2M_{12}M_{23}[r\omega^2({M_{23}}^2 - {M_{13}}^2) + (r^2 + \omega^2{M_{12}}^2)(r_3 + R_L)] \\ h = r\omega M_{13}[r\omega^2({M_{13}}^2 + {M_{23}}^2) + (r^2 + \omega^2{M_{12}}^2)(r_3 + R_L)] + 2\omega^5{M_{12}}^2M_{13}{M_{23}}^2 \end{cases} \tag{A.3}$$

REFERENCES

[1] D. Ahn and S. Hong, "Wireless power transmission with self-regulated output voltage for biomedical implant," *IEEE Trans. Ind. Electron.*, vol. 61, no. 5, pp. 2225–2235, May 2014.

[2] Z. Cheng *et al.*, "Design and loss analysis of loosely coupled transformer for an underwater high-power inductive power transfer system," *IEEE Trans. Magn.*, vol. 51, no. 7, pp. 1–10, Jul. 2015.

[3] Y. Jang and M. M. Jovanovic, "A contactless electrical energy transmission system for portable-telephone battery chargers," *IEEE Trans. Ind. Electron.*, vol. 50, no. 3, pp. 520–527, Jun. 2003.

[4] C. Zheng *et al.*, "High-efficiency contactless power transfer system for electric vehicle battery charging application," *IEEE J. Emerg. Sel. Topics Power Electron.*, vol. 3, no. 1, pp. 65–74, Mar. 2015.

[5] S. Y. Choi *et al.*, "Advances in wireless power transfer systems for roadway-powered electric vehicles," *IEEE J. Emerg. Sel. Topics Power Electron.*, vol. 3, no. 1, pp. 18–36, Mar. 2015.

[6] J. T. Boys and G. A. Covic, "The inductive power transfer story at the University of Auckland," *IEEE Circuits Syst. Mag.*, vol. 15, no. 2, pp. 6–27, May 2015.

[7] J. M. Miller *et al.*, "ORNL experience and challenges facing dynamic wireless power charging of EV's," *IEEE Circuits Syst. Mag.*, vol. 15, no. 2, pp. 40–53, May 2015.

[8] J. H. Kim *et al.*, "Development of 1-MW inductive power transfer system for a high-speed train," *IEEE Trans. Ind. Electron.*, vol. 62, no. 10, pp. 6242–6250, Oct. 2015.

[9] A. Berger *et al.*, "A wireless charging system applying phase-shift and amplitude control to maximize efficiency and extractable power," *IEEE Trans. Power Electron.*, vol. 30, no. 11, pp. 6338–6348, Nov. 2015.

[10] Z.-H. Ye *et al.*, "Energy efficiency analysis of u-coil wireless power transfer system," *IEEE Trans. Power Electron.*, vol. 31, no. 7, pp. 4809–4817, Sep. 2015.

[11] H. Li, J. Li, K. Wang, W. Chen, and X. Yang, "A maximum efficiency point tracking control scheme for wireless power transfer systems using magnetic resonant coupling," *IEEE Trans. Power Electron.*, vol. 30, no. 7, pp. 3998–4008, Jul. 2015.

[12] D. Kobayashi, T. Imura, and Y. Hori, "Real-time coupling coefficient estimation and maximum efficiency control on dynamic wireless power transfer for electric vehicles," in *Proc. 2015 IEEE PELS Workshop Emerging Technologies: Wireless Power*, Jun. 2015, pp. 1–6.

[13] W. X. Zhong and S. Y. R. Hui, "Maximum energy efficiency tracking for wireless power transfer systems," *IEEE Trans. Power Electron.*, vol. 30, no. 7, pp. 4025–4034, Jul. 2015.

[14] T. Diekhans and R. W. De Doncker, "A dual-side controlled inductive power transfer system optimized for large coupling factor variations and partial load," *IEEE Trans. Power Electron.*, vol. 30, no. 11, pp. 6320–6328, Nov. 2015.

[15] A. Berger, M. Agostinelli, S. Vesti, J. A. Oliver, J. A. Cobos, and M. Huemer, "A wireless charging system applying phase-shift and amplitude control to maximize efficiency and extractable power," *IEEE Trans. Power Electron.*, vol. 30, no. 11, pp. 6338–6348, Nov. 2015.

[16] R. Johari, J. Krogmeier, and D. Love, "Analysis and practical considerations in implementing multiple transmitters for wireless power transfer via coupled magnetic resonance," *IEEE Trans. Ind. Electron.*, vol. 61, no. 4, pp. 1774–1783, Apr. 2014.

[17] F. Jolani, Y.-Q. Yu, and Z. Chen, "A planar magnetically-coupled resonant wireless power transfer using array of resonators for efficiency enhancement," in *Proc. IEEE Int. Microwave Symp.*, 2015, pp. 1–4.

[18] S. Huh and D. Ahn, "Two-transmitter wireless power transfer with optimal activation and current selection of transmitters," *IEEE Trans. Power Electron.*, vol. 33, no. 6, pp. 4957–4967, Jun. 2018.

[19] D. Ahn and S. Hong, "Effect of coupling between multiple transmitters or multiple receivers on wireless power transfer," *IEEE Trans. Ind. Electron.*, vol. 60, no. 7, pp. 2602–2613, Jul. 2013.

[20] I.-J. Yoon and H. Ling, "Investigation of near-field wireless power transfer under multiple transmitters," *IEEE Antennas Wireless Propag. Lett.*, vol. 10, pp. 662–665, Jun. 2011.

[21] B. Choi, J. Kim, J. Cheon, and C. Rim, "Synthesized magnetic field focusing using a current-controlled coil array," *IEEE Magn. Lett.*, vol. 7, Feb. 2016, Art. no. 6501504.

[22] P. Kong and H. Ku, "Efficiency optimizing scheme for wireless power transfer system with two transmitters," *Electron. Lett.*, vol. 52, no. 4, pp. 310–312, Feb. 2016.

[23] J. Wu *et al.*, "A new dual-bridge series resonant DC–DC converter with dual tank," *IEEE Trans. Power Electron.*, vol. 33, no. 5, pp. 3884–3897, May 2018.

[24] A. Zaheer, G. A. Covic, and D. Kacprzak, "A bipolar pad in a 10-kHz 300-W distributed IPT system for AGV applications," *IEEE Trans. Ind. Electron.*, vol. 61, no. 7, pp. 3288–3301, Jul. 2014.

Ruikun Mai (M'14) received the B.Sc. and Ph.D. degrees in electrical engineering from the School of Electrical Engineering, Southwest Jiaotong University, Chengdu, China, in 2004 and 2010, respectively.

He is currently a Professor with the School of Electrical Engineering, Southwest Jiaotong University. His research interests include wireless power transfer and its application in railway systems and power system stability and control.

Zhaotian Yan received the B.Sc. degree in electrical engineering and automation from the School of Electrical Engineering, Southwest Jiaotong University, Chengdu, China, in 2018, where he is currently working toward the Ph.D. degree.

His main research interest includes wireless power transfer.

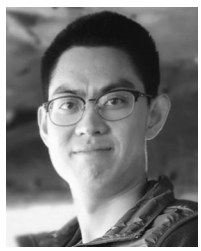

Yang Chen (S'17) received the B.Sc. degree in electrical engineering and automation from the School of Electrical Engineering, Southwest Jiaotong University, Chengdu, China, in 2015, where he became a master's student since September 2015. He is currently working toward the Ph.D. degree. In 2018, he received the scholarship under the State Scholarship Fund of China Scholarship Council, and became a joint Ph.D. student with the Future Energy Electronics Center (FEEC), Virginia Tech, Blacksburg, VA, USA.

His research interests include wireless power transfer, especially on compensation topology and misalignment tolerance improvement.

Shunpan Liu received the B.S. degree in electrical engineering and automation from the School of Electrical Engineering, Southwest Jiaotong University, Chengdu, China, in 2018, where he is currently working toward the Ph.D. degree.

His main research interest includes wireless power transfer.

Zhengyou He (M'10–SM'13) received the B.S. and M.S. degrees from the Chongqing University, Chongqing, China, in 1992 and 1995, respectively, and the Ph.D. degree from the Southwest Jiaotong University, Chengdu, China, in 2001.

Since 2002, he has been a Professor with the School of Electrical Engineering, Southwest Jiaotong University. He was a Visiting Scholar with the Cornell University, Ithaca, NY, USA, from 2008 to 2009. His research interests include signal processing and information theory and its application in electrical power systems, and the application of wavelet transforms in power systems.